Acta Geophysica
https://doi.org/10.1007/s11600-021-00720-4

RESEARCH ARTICLE - APPLIED GEOPHYSICS

P-Impedance and V_p/V_s prediction based on AVO inversion scheme with deep feedforward neural network: a case study from tight sandstone reservoir

Xinjun Mao[1] · Xuehui Han[2] · Baohai Wu[3] · Zhenlin Wang[4] · Hao Zhang[1] · Hongliang Wang[5]

Received: 25 May 2021 / Accepted: 21 December 2021

Abstract
The low-frequency component of seismic data is an inevitable part to obtain absolute *P*-impedance (I_p) and V_p/V_s ratio of the subsurface, especially for the reservoir sweet spot. In this work, we train the deep feedforward neural network (DFNN) with band-pass seismic data and well log data to obtain favorable low-frequency components. Specifically, the Bayesian inference strategy is first applied to the pre-stack constrained sparse spike inversion process, obtaining an "initial" inverted band-pass parameters, which are subsequently used as input when applying the DFNN algorithm to predict low- and band-pass parameters. Moreover, the high linear correlation coefficient between the DFNN-based inversion results and the realistic well logging curves of the blind wells demonstrates that the DFNN-based inversion scheme exhibits strong robustness and good generalization ability. Ultimately, we apply the proposed DFNN-based inversion strategy to a tight sandstone reservoir located at the Sichuan basin field from onshore China. Both low- and band-pass I_p and V_p/V_s inverted for the clastic formation of the Sichuan basin show a strong correlation with the corresponding I_p and V_p/V_s logs.

Keywords *P*-Impedance · V_p/V_s Ratio · AVO inversion · Deep feedforward neural network

Introduction

Both seismic inversion and rock physical modeling play significant roles in the quantitative seismic interpretation of reservoir properties. However, the frequencies of seismic data predominately are within the intermediate band, resulting in a relatively large uncertainty between relative seismic reflectivity and absolute elastic parameters when using seismic inversion (Ball et al. 2014; Yuan et al. 2019). Therefore, on the one hand, both empirical and model-based rock physical inversion workflows use the absolute elastic parameters as input (Doyen and Guidish 1992; Mukerji et al. 2001; Buland and Omre 2003; Eidsvik et al. 2004; Yuan et al. 2021). On the other hand, to obtain absolute parameters from the band-pass seismic data, a low-frequency portion of the elastic parameters is generally estimated using the well interpolation method.

Overall, the well-driven low-frequency model in seismic inversion process highly depends on well distribution, which mainly includes the homogeneity and the grid density of well distribution in the space. Moreover, it is risky to make a quantitative seismic interpretation because the horizontal trend of the low-frequency model might contradict the geological trend. Although the modified methods (e.g., trend-constrained interpolation) have been developed practically in the seismic interpretation, the "buphthalmos" artifact caused by well interpolation is still strong and is criticized by geologists and development engineers as well (Caers 2011; Deutsch 2002; Eidsvik et al. 2015).

Edited by Prof. Sanyi Yuan (ASSOCIATE EDITOR) / Prof. Michał Malinowski (CO-EDITOR-IN-CHIEF).

✉ Xinjun Mao
geosci_2020@126.com

1 Exploration department of Xinjiang Oilfield Company, PetroChina, Karamay 834000, China

2 School of Geoscience, China University of Petroleum (East China), Qingdao 266580, China

3 CGG, Beijing 100016, China

4 Research Institute of Petroleum Exploration and Development, Xinjiang Oilfield Company, PetroChina, Karamay 834000, China

5 CNPC West Drilling Engineering Company Limited, Ürümqi 830011, China

Published online: 04 March 2022

In the past, there are some documented investigations devoted to eliminating such discrepancy academically and industrially in rock physics and seismic domains. Ball et al. (2014) developed a relative rock physical framework to practically compute relative elastic properties. In some cases, note that empirical- and model-based relative rock physics framework provides us a possibility to avoid statistical complications associated with absolute elastic properties. However, it is mainly used to explain the elastic parameter variation (such as time-lapse seismic interpretation) and still cannot be directly applied to elastic parameters inversion because of the lack of completeness of solid theoretical basis. In addition, Mesdag et al. (2010) proposed a method of updating the low-frequency model to account for high contrast *P*-impedance layers. However, this updated low-frequency model is only feasible when the geologic/elastic anomaly with large contrast of P-impedance exists and is not a general solution for low-frequency model prediction.

In current times, with the rapid development of massive computational powers, novel data-driven machine learning approaches have been developed promptly to address various questions in diverse research domains (Monajemi et al. 2016). The deep neural network (DNN) is one of the most important machine learning applications. The factors affecting the DNN prediction results are mainly the number and quality of the training samples, the number of the hidden layers, and the numbers of neurons in each hidden layer. LeCun et al. (2015) and GoodFellow et al. (2016) claimed that DNN essentially establishes a mapping relation of output parameters and training datasets with multiple hidden layers. Lopez-Moreno et al. (2016) used deep feedforward neural networks (DFNN) to automatically identify the language.

Numerous DNN algorithms have been widely applied to the geoscience discipline and achieved successful applications. Specifically, using DNN to obtain seismic amplitude properties mainly concentrates on the following two aspects. First, the DNN algorithm is only applied to the sub-step of the conventional inversion framework. For example, Richardson (2018) used the recurrent neural network (RNN) to replace forward modeling and gradient calculation in the seismic full-waveform inversion. Second, DNN is directly used to obtain mapping relation from seismic amplitude dataset to elastic properties, implementing data-driven amplitude inversion (Alfarraj and AlRegib 2019; Das et al. 2019; Biswas et al. 2019; Di et al. 2020; Li et al. 2021). Araya-Polo et al. (2018) reconstructed the subsurface velocity model from synthetically generated seismic profiles using the DNN algorithm, instead of using the conventional inversion framework.

Note that using DNN (e.g., CNN) to predict elastic properties from seismic data generally requires massive training samples (Zheng and Zhang 2018). Consequently, DNN is more suitable for geoscience researchers to construct a model using a local training dataset, which comes from the reservoir area with a smooth variation in lateral stratigraphic structure (Peters et al. 2019). Compared with the intermediate- and high-frequency bands of the seismic data, the low-frequency components vary smoothly in the spatial distribution. As a result, DNN can be a powerful tool to build a low-frequency model from band-pass seismic data, leading to inverse absolute elastic parameters from the full-band dataset. Based on this strategy, we propose a hybrid algorithm strategy that combines pre-stack constrained sparse spike inversion with DFNN to obtain absolute elastic parameters (I_p and V_p/V_s) of tight sandstone gas reservoirs.

This paper is constructed as follows: first, we briefly introduce the pre-stack constrained sparse spike inversion theory. Second, a DFNN-based seismic inversion workflow is given. Third, a model test is given to testify the robustness of the proposed DFNN-based inversion workflow. Fourth, we applied the DFNN-based inversion workflow to the field data and obtained elastic parameters (I_p and V_p/V_s). Lastly, this paper ends with conclusions.

Theory and methodology

In this work, to estimate the elastic parameters (I_p and V_p/V_s) from the pre-stack seismic data, we propose a DFNN-based inversion workflow accordingly. It mainly includes two steps: the pre-stack constrained sparse spike inversion and DFNN-based elastic parameter prediction. Here, the band-pass elastic parameters (I_p and V_p/V_s) are first inverted from pre-stack seismic data using the pre-stack constrained sparse spike inversion. After that, the DFNN-based network is applied to estimate the corresponding low-frequency components of elastic parameters and extend the band-pass elastic parameters (I_p and V_p/V_s) into low- and band-pass elastic parameters (I_p and V_p/V_s). In the following subsection, we will detail them accordingly.

Pre-stack constrained sparse spike inversion

Pre-stack amplitude versus offset (AVO) inversion strategy is a primary technique in estimating elastic parameters of the subsurface reservoir with respect to seismic angle gathers. Noticeably, seismic reflectivity amplitudes resulting from the lithology contrast highly depend on the reflection angle and the elastic properties of rock lithology (Buland and Omre 2003; Connolly 1999; Kelly 2001; Russell et al. 2011).

Technically speaking, due to the noise effect and measurement uncertainty, the pre-stack constrained sparse spike inversion technique is an ill-posed and multidimensional problem. As a consequence, additional constraints are usually added to the AVO inversion procedure to obtain rational and reliable inversion results. In this work, like most other

geophysical inversion strategies, we cast pre-stack constrained sparse spike inversion into the Bayesian inference framework with respect to consideration of sparseness and scale matrix, which are preferable to improve the correlation between inverted parameters. Meanwhile, the Cauchy distribution is applied to describe the priori distribution of the reflectivity because the Cauchy distribution has the more convergent peak of probability density and distinct long-tail feature in the low probability zone comparing to typical Gaussian probability distribution. In addition, the sparse part in the objective function theoretically equals norm 1. However, it is due to the difficulty of the solution process and massive calculation burden; we use a linear programming method to constrain the solution of the objective function (Debeye and Vanriel 1990).

With known priori distribution and likelihood function, the posterior distribution of inverted parameters can be given as:

$$P(\mathbf{m}|\mathbf{d}) = \frac{P(\mathbf{d}|\mathbf{m})P(\mathbf{m})}{P(\mathbf{d})}, \tag{1}$$

where $P(\mathbf{d}|\mathbf{m})$ is a likelihood function, $P(\mathbf{m})$ is the priori distribution of the elastic parameters, $P(\mathbf{d})$ marginal probability distribution, m is objective inversion parameter, and d is the measured data. Here if we assume noise obeys the Gaussian distribution, then the likelihood function is given as:

$$P(\mathbf{d}|\mathbf{m}) = \frac{1}{(2\pi)^{N_d/2}\left|\mathbf{C_d}\right|^{1/2}}\left\{-\frac{1}{2}(\boldsymbol{\gamma}(\mathbf{d}-\mathbf{Lm})^T\mathbf{C_d^{-1}}((\boldsymbol{\gamma}(\mathbf{d}-\mathbf{Lm}))\right\}, \tag{2}$$

where $\mathbf{C_d}$ and N_d are covariance matrix and dimension of the measured data, respectively. $\boldsymbol{\gamma}$ is a diagonal matrix to adapt the empty feature of the measured data.

Combining with Cauchy distribution, then priori distribution can be given as:

$$P(\mathbf{m}) = \frac{1}{\pi^{2N}|\boldsymbol{\Psi}|^{N/2}}\left[-2\sum\nolimits_{i=1}^{N}\ln\left(1+\mathbf{m}^T\boldsymbol{\Phi}^i\mathbf{m}\right)\right], \tag{3}$$

where $\boldsymbol{\Phi}^i = (\mathbf{D}^i)^T\boldsymbol{\Psi}^{-1}\mathbf{D}^i$; the matrix $\boldsymbol{\Psi}$ is a 3×3 scale matrix. $\mathbf{D}^i$ denotes the $3\times(3N)$ matrix and is defined by:

$$\left[D^i_{nl}\right] = \begin{cases} 1, \text{ if } & n=1 \text{ and } l=i \\ 1, \text{ if } & n=2 \text{ and } l=i+N \\ 1, \text{ if } & n=3 \text{ and } l=i+2N \\ 0, \text{ others} & \end{cases}, \tag{4}$$

where N denotes the number of the sample points. n is 1, 2, and 3, respectively. l ranges from 1 to $3N$.

Finally, the posterior function is:

$$P(\mathbf{m}|\mathbf{d}) = \left\{-\frac{1}{2}(\boldsymbol{\gamma}(\mathbf{d}-\mathbf{Lm}))^{\mathbf{T}}\mathbf{C_d^{-1}}(\boldsymbol{\gamma}(\mathbf{d}-\mathbf{Lm})) - 2\sum\nolimits_{i=1}^{N}\ln\left(1+\mathbf{m}^T\boldsymbol{\Phi}^i\mathbf{m}\right)\right\}. \tag{5}$$

Solving the maximum of the posterior probability density function is mathematically equivalent to find the minimum of

$$J(\mathbf{m}) = \frac{1}{2}(\boldsymbol{\gamma}(\mathbf{d}-\mathbf{Lm}))^T\mathbf{C}_d^{-1}(\boldsymbol{\gamma}(\mathbf{d}-\mathbf{Lm})) + R(\mathbf{m}), \tag{6}$$

where $R(\mathbf{m}) = 2\sum_{i=1}^{N}\ln\left(1+\mathbf{m}^T\boldsymbol{\Phi}^i\mathbf{m}\right)$. Here, $R(\mathbf{m})$ is a regular term of the Cauchy distribution (detailed in Appendix A). Therefore, finding the minimum of $J(\mathbf{m})$ is equivalent to solve:

$$\left(\mathbf{L}^T\boldsymbol{\gamma}^T\mathbf{C}_d^{-1}\boldsymbol{\gamma}\mathbf{L} + 2\mathbf{Q}_{kn}\right)\mathbf{m} = \mathbf{L}^T\boldsymbol{\gamma}^T\mathbf{C}_d^{-1}\boldsymbol{\gamma}\mathbf{d}, \tag{7}$$

where

$$Q_{kn} = \sum\nolimits_{i=1}^{N}\frac{2\boldsymbol{\Phi}^i_{kn}}{1+\mathbf{m}^T\boldsymbol{\Phi}^i\mathbf{m}},\ k,n = 1,2,3,\ldots,3N. \tag{8}$$

If $\mathbf{C}_d^{-1} = \frac{1}{\sigma_d^2}\mathbf{I}$, σ_d^2 is noise variance, $\mathbf{I}$ is a unit matrix, substituting these into Eq. (8) to get:

$$\left(\mathbf{L}^T\boldsymbol{\gamma}^T\boldsymbol{\gamma}\mathbf{L} + \mu\mathbf{Q}\right)\mathbf{m} = \mathbf{L}^T\boldsymbol{\gamma}^T\boldsymbol{\gamma}\mathbf{d}, \tag{9}$$

where $\mu \sim \sigma_d^2$. μ is a hyper-parameter.

Finally, the weighted iterative least square method is applied to solve Eq. (9), obtaining the inverted parameters.

Architecture of DFNN model

In this work, the DFNN takes the band-pass (12–45 Hz) I_p and V_p/V_s obtained by pre-stack constrained sparse spike inversion as an input and the actual high-cut (45/5 Hz) log curves as the target output to train a stable DFNN model (Fig. 1). Then, the well-trained DFNN model is used to predict the low- and band-pass (0–45 Hz) elastic properties (e.g., I_p and V_p/V_s).

It is well known that the structure of the DFNN model has a significant impact on the prediction results. Therefore, it is necessary to determine the input of the neural network model, the number L of layers of the model, the number of neurons in each hidden layer, and the types of activation functions. Here, the network contains five layers in total. The first layer is the input layer, the 5th layer is the output layer, and the three middle layers are hidden layers. The number of neurons in each hidden layer is set to 20. In addition, it also needs to determine the learning rate η, the maximum Max of iterations, and stop the iterative threshold ε in advance. Normally, the learning

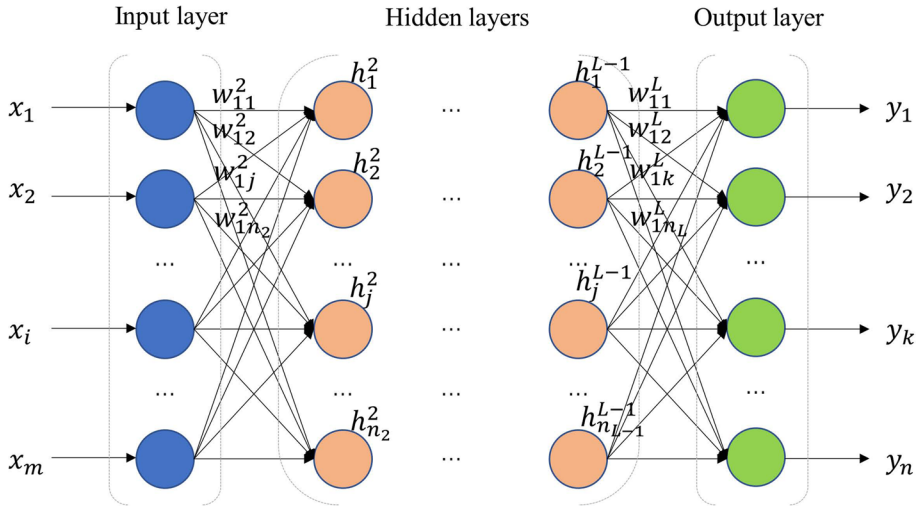

Fig. 1 Overall structure of DFNN

rate η is a small value, and the learning rate η is set to 0.001 in this paper. The maximum *Max* of iterations is set to 200. The sum of the squared errors of the output layer is as the objective function:

$$\text{Loss} = \frac{\sum_{i=1}^{N} \left(\mathbf{m}_{\text{predicted}} - \mathbf{m}_{\text{target}}\right)^2}{N}, \tag{10}$$

where $\mathbf{m}_{\text{predicted}}$ represents the elastic parameters predicted by the DFNN, $\mathbf{m}_{\text{target}}$ is the corresponding label, N is the number of sampling points of the logging curve.

Then, the gradient-based optimization algorithm is used to minimize the proposed objective function through iterative updating of the parameters of the network (Fig. 2). The algorithm flow is as follows:

Step 1 Small random numbers are used to initialize the weights, and training time t is set to 0.

Step 2 A training sample $\mathbf{x} = [x_1, x_2, \ldots, x_n]^T \in \mathbf{R}^n$ is obtained from the training set, and its expected output $\mathbf{D}_{output}$ is $[d_1, d_2, \ldots, d_n]^T \in \mathbf{R}^m$. Samples are usually selected from the training set in an arbitrary order.

Step 3 Calculate the actual output of the current neural network when $\mathbf{x}$ is input.

$$y_r = f\left(\sum_{s=1}^{n_{L-1}} w_{sr}^{l=L} \cdots f\left(\sum_{j=1}^{n_2} w_{jk}^{l=3} f\left(\sum_{i=1}^{n_1} w_{ij}^{l=2} x_i\right)\right)\right),\ r = 1, \ldots, m, \tag{11}$$

where w_{ij}^l represents the connection weight of the *ith* neuron of the $(l-1)$th layer and the *j*th neuron of the *l*th

Fig. 2 Algorithm workflow of DFNN

Input: sample x and the expected output D corresponding to sample x

Output: The result y calculated by network model

1. Initialize the W of each hidden layer and output layer
2. for $t = 0 : Max$
   (1) for $i = 1{:}m$
   (a) Calculate the actual output of the current neural network

$$y_r = f\left(\sum_{s=1}^{n_{L-1}} w_{sr}^{l=L} \cdots f\left(\sum_{j=1}^{n_2} w_{jk}^{l=3} f\left(\sum_{i=1}^{n} w_{ij}^{l=2} x_i\right)\right)\right),$$
$$r = 1, \ldots, m$$

   (b) Calculate the error δ_j^l of the output layer and the hidden layers
   (c) Adjust the weights from the output layer

$$w_{ij}^l(t+1) = w_{ij}^l(t) + \Delta w_{ij}^l(t),$$
$$l = 2, \ldots, L, j = 1, \ldots, n_l, i = 1, \ldots, n_{l-1}$$

   (2) If error between the output of updated network and the expected output is less than the stop iteration threshold ε, then the iteration loop is jumped out. Otherwise set $t = t + 1$ and return (1).

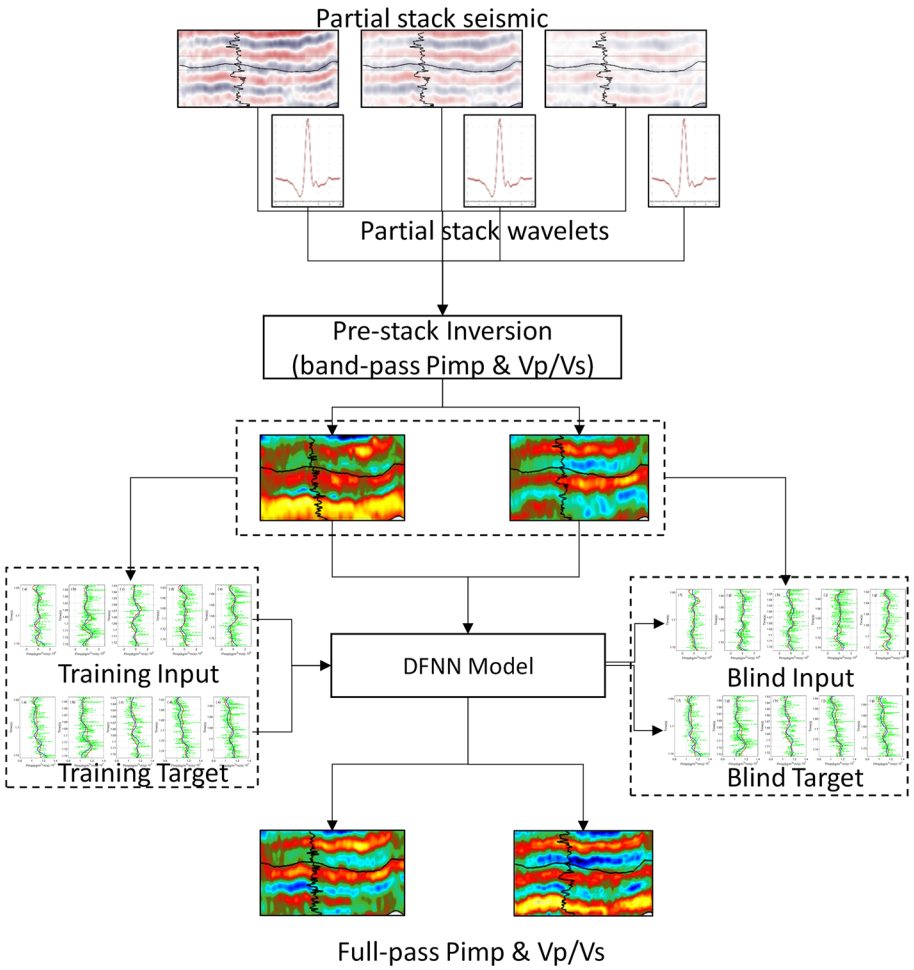

Fig. 3 Workflow of AVO inversion-DFNN hybrid algorithm for low- and band-pass I_p and V_p/V_s prediction

layer, $l = 2, \ldots, L$. y_r is the output of the *rth* neuron of the output layer. $f(\cdot)$ is the sigmoid activation function.

$$f(x) = \frac{1}{1 + e^{-x}}. \tag{12}$$

Step 4 Adjust the weights from the output layer. For the *lth* layer, the following formula is used to update the weight.

$$w_{ij}^{l}(t+1) = w_{ij}^{l}(t) + \Delta w_{ij}^{l}(t), l = 2, \ldots, L, j = 1, \ldots, n_l, i = 1, \ldots, n_{l-1}, \tag{13}$$

where $\Delta w_{ij}^{l}(t)$ is the weight correction term. It is defined by:

$$\Delta w_{ij}^{l}(t) = \eta \delta_j^l x_{ij}^l, \tag{14}$$

where x_{ij}^l is the input from the ith neuron of the $(l-1)$th layer to the ith neuron of the lth layer. For the output layer $(l = L)$, the error δ_j^l of jth neuron is calculated as follows:

$$\delta_j^l = y_j(1 - y_j)(d_j - y_j), j = 1, \ldots, m, \tag{15}$$

where d_j and y_j are the expected output and the output calculated by the model of the *jth* neuron, respectively. The hidden layer $(l = 2, \ldots, L-1)$ δ_j^l is calculated according to:

$$\delta_j^l = h_j^l\left(1 - h_j^l\right) \sum_{k=1}^{n_{l+1}} \delta_k^{l+1} w_{jk}^{l+1}(t), j = 1, \ldots, n_{l-1}, \tag{16}$$

where h_j^l is the output of the jth neuron of the lth layer.

Step 5 After updating all weights, the outputs are recalculated for all training samples, and the error between the output of the updated network and the expected output is calculated. If the convergence condition is reached, stop iteration, otherwise set $t = t + 1$ and return step 2.

Workflow of DFNN-based inversion

As shown in Fig. 3, there exist two primary steps to perform elastic parameters inversion from pre-stack seismic

data. Band-pass parameters inversion is first conducted in the designed workflow. It has been well known that input parameters of pre-stack inversion include partial stacking seismic and corresponding wavelets. Note that the quality of the stacking seismic dataset and the extracted wavelets mainly determines the frequency band of the inverted elastic parameters. In a conventional pre-stack inversion, the low-frequency components of elastic parameters from well interpolation are another input. Second, the full-band pass parameters (e.g. I_p, V_p/V_s) are consequently obtained by merging low-frequency components with band-pass components in the frequency domain. Here, instead of using the conventional well-interpolation method, the following DFNN-based algorithm is applied to estimate the low-frequency components of elastic parameters.

Next, the DFNN algorithm is applied to obtain low-frequency components of the dataset. In this step, the output I_p and V_p/V_s are learned separately. I_p and V_p/V_s are just using common network structures as shown in Fig. 1. The training samples include two parts: (1) the training input of DFNN and (2) the training label. To acquire sufficient training samples, more than 20 attributes were actually computed and ranked according to their relevance to the target quantity (I_p and V_p/V_s) during the sensitive attribute selection. For I_p, the following five attributes including amplitude weighted consin phase (Pimp_bp), filter 5/10–15/20 (Pimp_bp), $(\text{Pimp\_bp})^2$, apparent polarity (Pimp_bp), and amplitude weighted phase (Pimp_bp) are considered as training samples in this work. For V_p/V_s, the following five attributes including integrate (Vp/Vs_bp), quadrature trace (Vp/Vs_bp), amplitude weighted frequency (Vp/Vs_bp), filter 5/10–15/20 (Vp/Vs_bp), and $(\text{Vp/Vs\_bp})^2$) are used as training samples in this work. It is because that there is the highest linear correlation coefficient with the low and band-pass (0–45 Hz) logging elastic curves. Meanwhile, to ensure the stability of the DFNN algorithm, we perform the high-cut (45/5 Hz) filter to the log curves subjecting to the upper limit of band-pass (12–45 Hz) parameters obtained by pre-stack inversion, retaining low- and band-pass (0–45 Hz) components of the dataset as training samples.

After setting the hyper-parameters, such as the number of hidden layers, the neurons of each hidden layer, and iteration number, the training samples are used to train the DFNN model. When the DFNN model is stable, the blind dataset is used to verify the robustness and generalization of the well-trained model. Specifically, here, we evaluate the robustness and generalization of the DFNN model from two angles. First, as shown in Figs. 4 and 5, the training loss curve converges fast, and the loss value after the final convergence is also smaller. Therefore, to some extent, it demonstrates that the DFNN model tends to be stable with 200 epochs. Second, the testing on both well logging data and field data using the DFNN model can also prove that the DFNN model is stable. Ultimately, we apply the DFNN model to directly estimate both low- and band-pass results from seismic data. It needs to point out that we use the inverted band-pass parameters from pre-stack constrained sparse spike inversion as the initial input of the DFNN model.

DFNN algorithm test

DFNN algorithm in this paper, the band-pass (12–45 Hz) component of the elastic log curves is used to predict the low- and band-pass (0–45 Hz) elastic parameters (I_p and V_p/V_s) in 10 wells. Here, 10 wells had been classified into two groups, 5 training wells, and 5 validation wells.

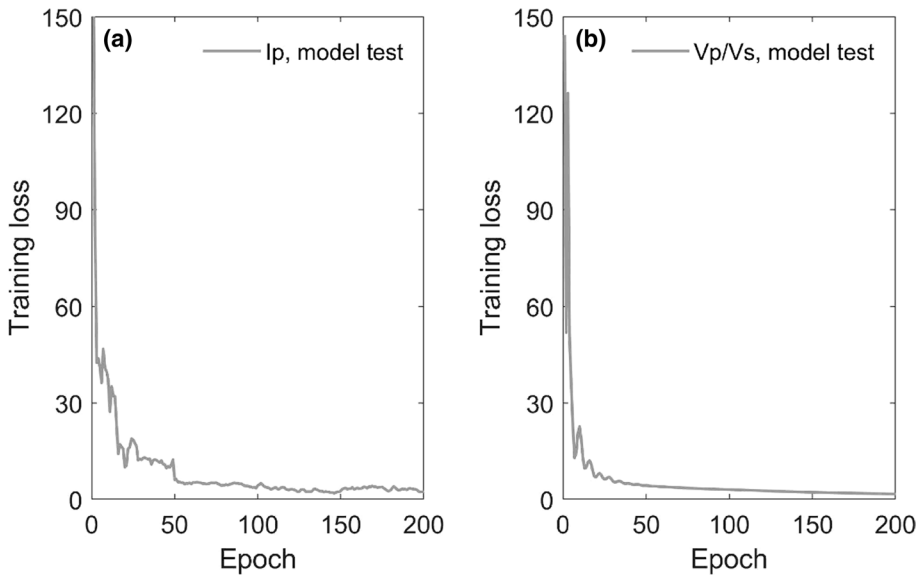

Fig. 4 Training loss with varying epoch for model test using the DFNN model

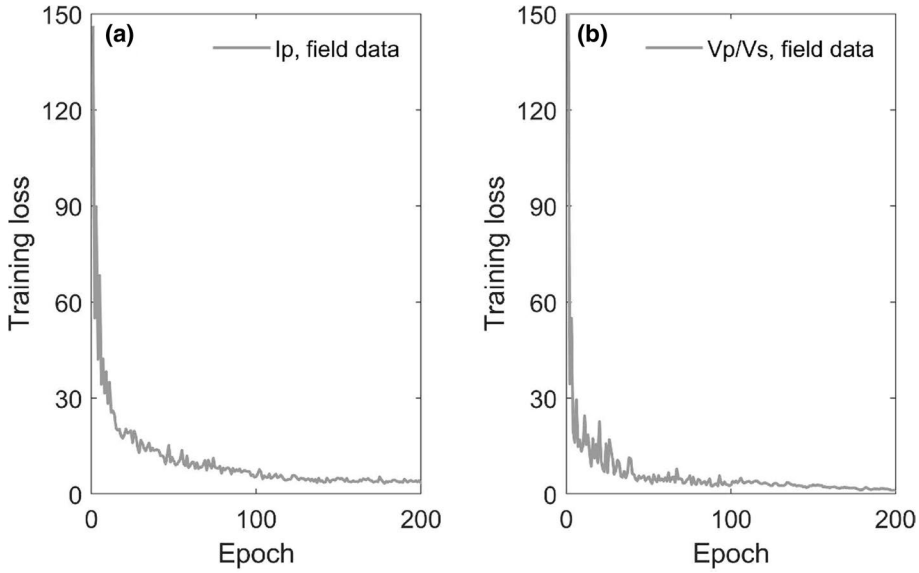

Fig. 5 Training loss with varying epochs for realistic data using the DFNN model

First, we perform the filtering on I_p and V_p/V_s in 5 training wells in the frequency domain. The input curves (band-pass elastic log curves, 12 /2–45 /5 Hz) and target logging curves (high-cut log curves, 0 ~45 Hz/5 Hz) in the DFNN training process are obtained, respectively. Second, to increase the sample abundance, the input training samples for the DFNN model are transformed into various seismic attributes. Here, those seismic attributes, which show the highest linear correlation coefficients with the labeled attributes, are used as the input accordingly. Then, the DFNN model is used to predict the output parameters (low- and band-pass I_p and V_p/V_s) from the input (band-pass I_p and V_p/V_s). The calculation iteration will terminate when the DFNN output has a high correlation with the target curves. Finally, the well-trained DFNN model is applied to another five blind wells to verify the generalization of the model.

In Fig. 6a–e, the green dashed curve is the original I_p log curve with low-cut (12/2 Hz). The blue solid curve is the original I_p log curve with a band-pass filter (12/2–45/5 Hz) (DFNN input). In Fig. 6f–j, the green dashed curve is the original elastic curve. The blue solid curve is the original log curve with a high-cut filter (45/5 Hz). The red solid curve is the low- and band-pass (0–45 Hz) results using DFNN model. As we can see, the correlation coefficient between the results predicted by DFNN and the high-cut (45/5 Hz) curve of the original log is high (Table 1), which proves the rationality of the DFNN for training wells. Moreover, the DFNN model is applied to 5 (posterior) blind wells to test the generalization of DFNN as shown in Fig. 7. Besides, Figs. 8, 9 display the V_p/V_s ratio predicted from (priori) training wells and (posterior) blind wells using the DFNN algorithm. The correlation coefficients in Table 1 suggest that DFNN is feasible in V_p/V_s prediction as well. However, the correlation between the DFNN-based prediction results and the band-pass filtering results is relatively low when the time is larger than 1.72 s which may be caused by the abnormal reflection of the coal seam or calcareous mudstone.

Field data example

To testify the feasibility of the proposed workflow in Fig. 3, we applied this AVO-DFNN hybrid inversion workflow to the clastic formation, Sichuan basin, China. Since the 3D seismic full folding in the studied area is about 400 km^2, and well log data are abundant, the dataset satisfies the requirement of predicting low-frequency components using band-pass parameters obtained by pre-stack constrained sparse spike inversion.

Pre-stack inversion

It is necessary to prepare some related preliminary work before performing pre-stack constrained sparse spike inversion. We first obtain five partial stack seismographs by stacking 3D common-reflection-point (CRP) gathers. Next, we pick ten wells with good measurement conditions to complete data pre-processing (e.g., environmental correction, multiple well normalizations). Because well C shows a high correlation between CRP gather and synthetic gather, it is suitably used to estimate wavelets.

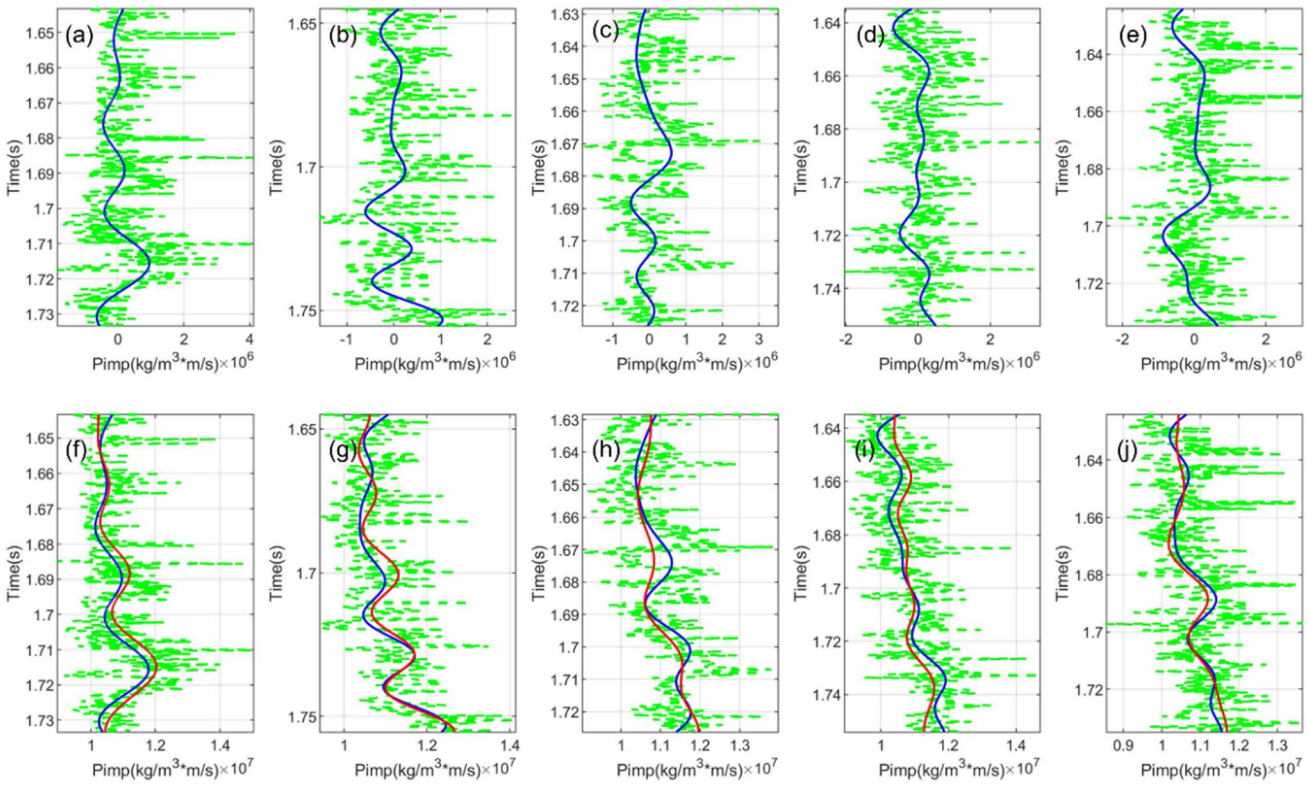

Fig. 6 I_p from (prior) five training wells (A–E). **a–e** Shows the original I_p log curve with low-cut (12/2 Hz) (green dashed line) and I_p log curve with a band-pass filter (12/2–45/5 Hz) (blue solid line) for these five training wells (A-E); **f–j** shows the original elastic curve (green dashed line) and the original log curve with a high-cut filter (45/5 Hz) (blue solid line) and the low- and band-pass (0–45 Hz) results using DFNN (red solid line)

Table 1 Correlation coefficient between high-cut log parameters and low- and band-pass parameters predicted by the DFNN model

Log number	The correlation coefficient between high-cut log I_p and low- and band-pass I_p predicted by DFNN	The correlation coefficient between high-cut log V_p/V_s and low- and band-pass V_p/V_s predicted by DFNN
Well A	0.802	0.891
Well B	0.718	0.942
Well C	0.095	0.792
Well D	0.598	0.943
Well E	0.147	0.911
Well F	0.415	0.855
Well G	0.564	0.508
Well H	0.202	0.827
Well I	0.317	0.881
Well J	0.357	0.838

Moreover, wavelets are extracted from partial stacking seismographs as shown in Fig. 10a. As we can see, the morphological features of the wavelets 1–3 estimated from small incident to middle angle gathers show a relatively high correlation comparing to that of wavelets 4–5, suggesting that there exists a high correlation well-seismic tie for wavelets 1–3. In addition, Fig. 10b displays that the amplitudes of the wavelets decrease with increasing incident angle. The comparability of wavelets 1–3 is relatively high comparing to the others. Consequently, we decide to

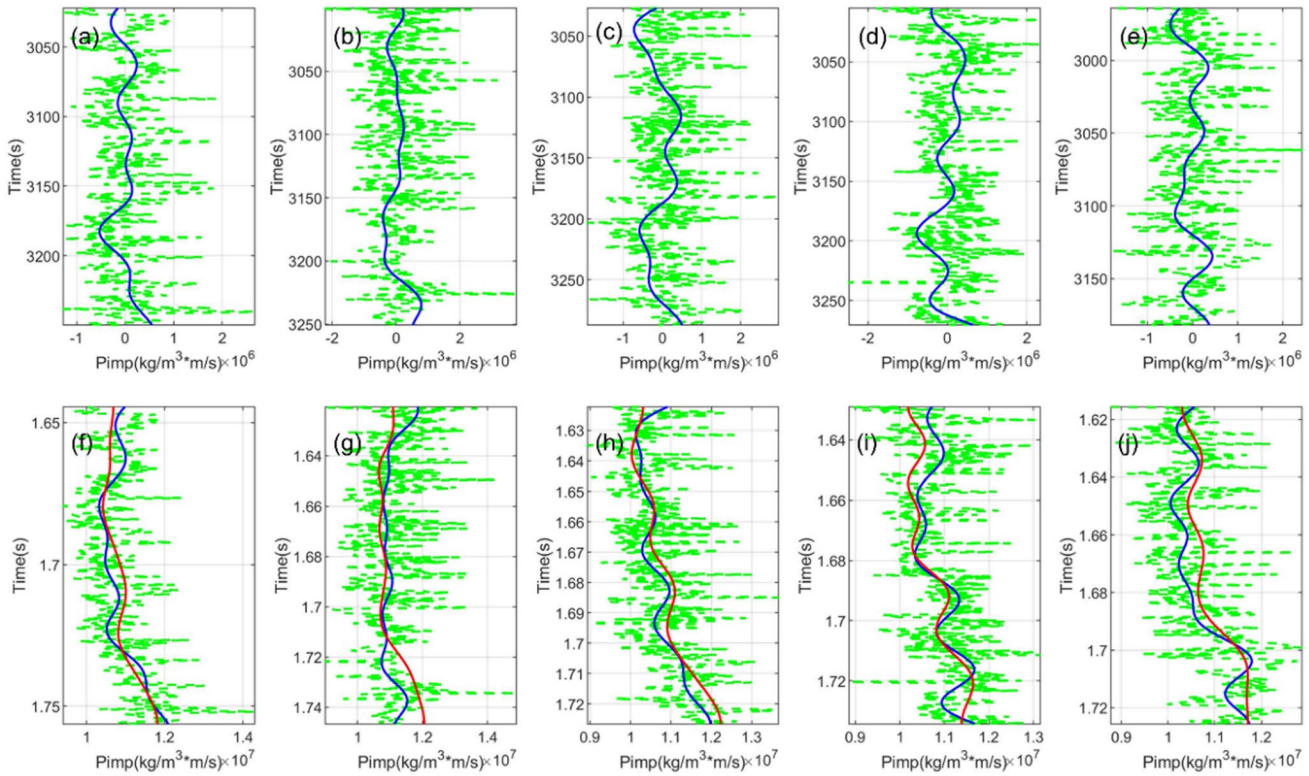

Fig. 7 I_p from (posterior) five blind wells (F–J). **a**–**e** shows the original I_p log curve with low-cut (12/2 Hz) (green dashed line) and I_p log curve with a band-pass filter (12/2–45/5 Hz) (blue solid line) for these five blind wells (A–E); **f**–**j** shows the original elastic curve (green dashed line) and the original log curve with a high-cut filter (45/5 Hz) (blue solid line) and the low- and band-pass (0–45 Hz) results using DFNN (red solid line)

use the first three stacking gathers and wavelets 1–3 as input to perform I_p and V_p/V_s inversion concerning the constrain of Cauchy distribution and scale matrix.

Figure 11 shows band-pass (12–45 Hz) I_p inverted from pre-stack seismic gather and band-pass (12–45 Hz) log curves, respectively. Note that the green dashed line denotes the original log curve with low-cut (12/2 Hz). The blue solid line indicates the original log curve with band-pass (12/2–45/5 Hz). The red solid line shows the inverted I_p from pre-stack band-pass seismic. In addition, Fig. 12 shows band-pass V_p/V_s inverted from seismic (12–45 Hz) and band-pass (12–45 Hz) log curves, respectively. At the seismic frequency band (12/2–45/5 Hz), the correlation between inverted parameters (I_p and V_p/V_s) and ones at the well site (band-pass log curve) is high, which, to a certain degree, ensures the reliability of seismic inversion.

DFNN model training

For DFNN model training, wells A–E and wells F–J in Fig. 13 are used to be training wells and verification wells, respectively. The low- and band-pass (0–45 Hz) I_p and Vp/Vs parameters are estimated using the DFNN algorithm. As stated above, based on inverted band-pass (12–45 Hz) I_p, the related attributes are calculated to satisfy the sample training requirement. Comparing these transformed attributes with those coming from low- and band-pass (0–45 Hz) I_p at well site, six attributes including amplitude weighted consin phase, filter 5/10–15/20 (Pimp_bp), $(\text{Pimp\_bp})^2$, time, apparent polarity (Pimp_bp), and amplitude weighted phase (Pimp_bp) are selected to be sample input because of high correlation.

Figure 13a–e, displays the low- and band-pass (0–45 Hz) I_p using the DFNN algorithm with respect to band-pass I_p obtained by pre-stack inversion as input on (priori) training wells. Note that green, blue, and red represent the original log curve, low- and band-pass (0–45 Hz) log curve, and low- and band-pass (0–45 Hz) I_p using DFNN prediction concerning band-pass I_p obtained by pre-stack inversion as input. Figure 13f–j displays the low- and band-pass I_p using DFNN prediction on (posterior) blind wells concerning band-pass I_p obtained by pre-stack inversion as input, verifying the DFNN's generalization capability. The correlation coefficient between inverted low- and band-pass I_p using DFNN (red) and low- and band-pass (45/5 Hz) I_p (blue) is shown

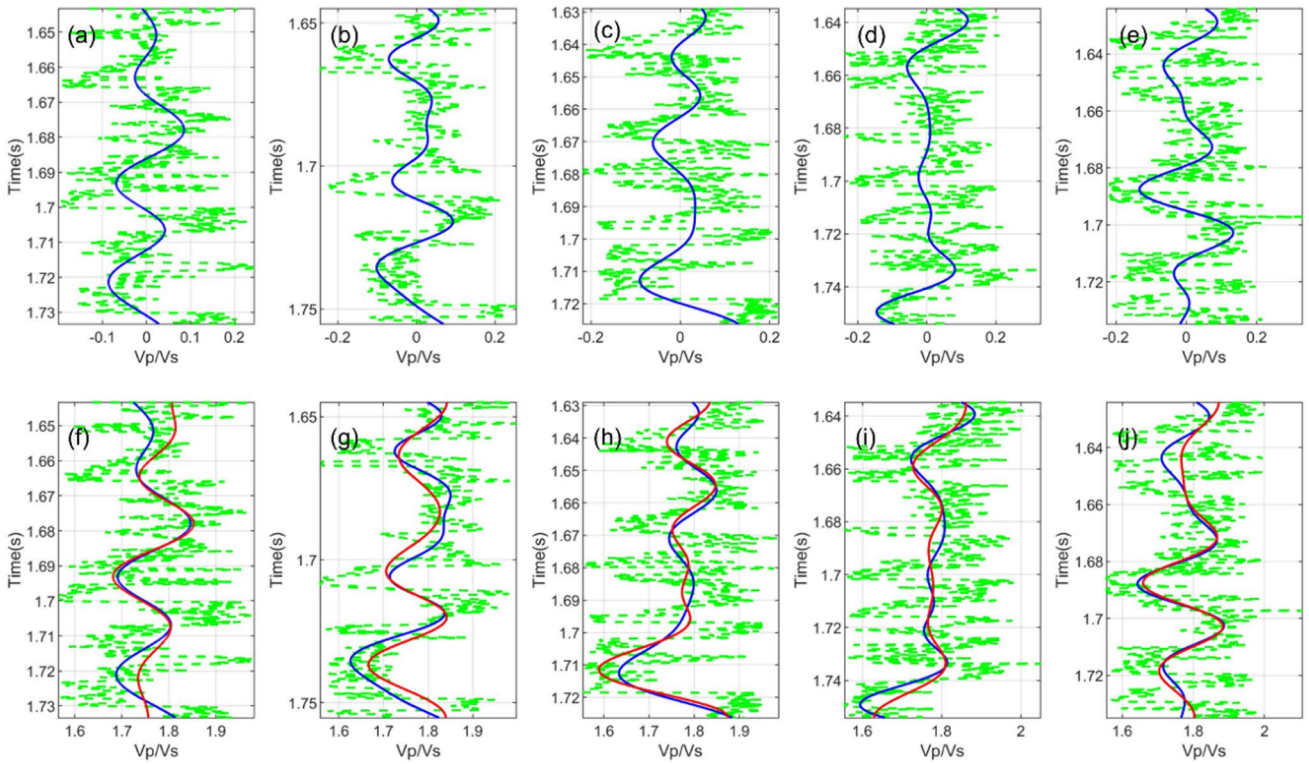

Fig. 8 V_p/V_s from (prior) five training wells (A–E). **a**–**e** shows the original V_p/V_s log curve with low-cut (12/2 Hz) (green dashed line) and V_p/V_s log curve with a band-pass filter (12/2–45/5 Hz) (blue solid line) for these five training wells (A–E); **f**–**j** shows the original elastic curve (green dashed line) and the original log curve with a high-cut filter (45/5 Hz) (blue solid line) and the low- and band-pass (0–45 Hz) results using DFNN (red solid line)

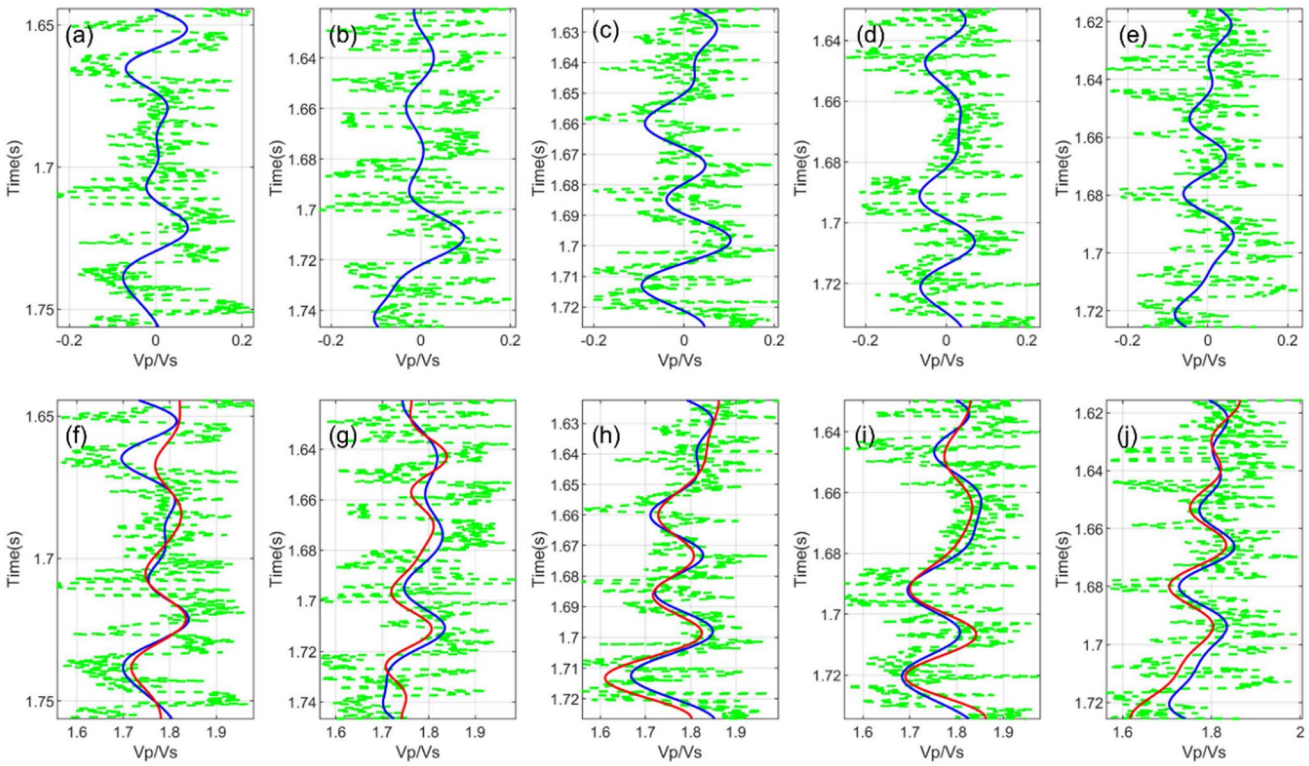

Fig. 9 V_p/V_s from (posterior) five blind wells (F–J). **a**–**e** shows the original V_p/V_s log curve with low-cut (12/2 Hz) (green dashed line) and V_p/V_s log curve with a band-pass filter (12/2–45/5 Hz) (blue solid line) for these five blind wells (A–E); **f**–**j** shows the original elastic curve (green dashed line) and the original log curve with a high-cut filter (45/5 Hz) (blue solid line) and the low- and band-pass (0–45 Hz) results using DFNN (red solid line)

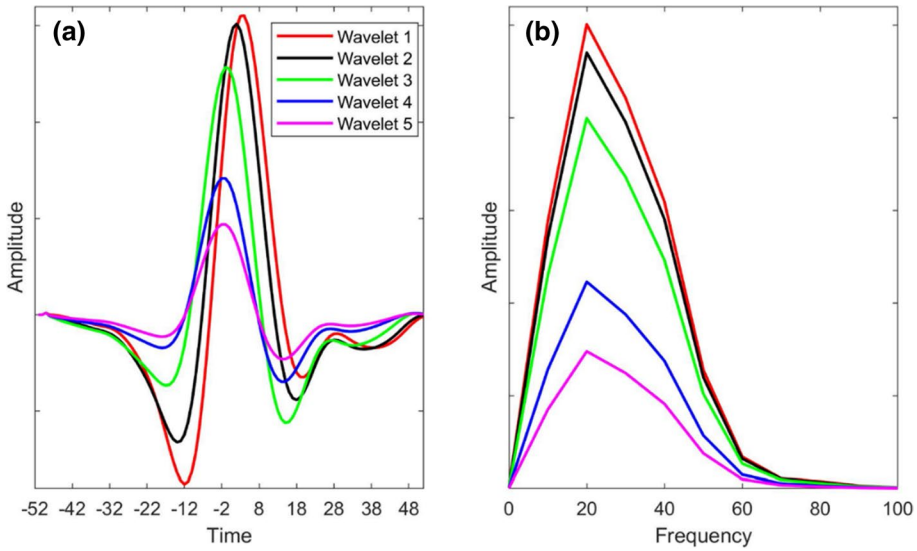

Fig. 10 **a** Extracted wavelets and **b** corresponding amplitude spectrum

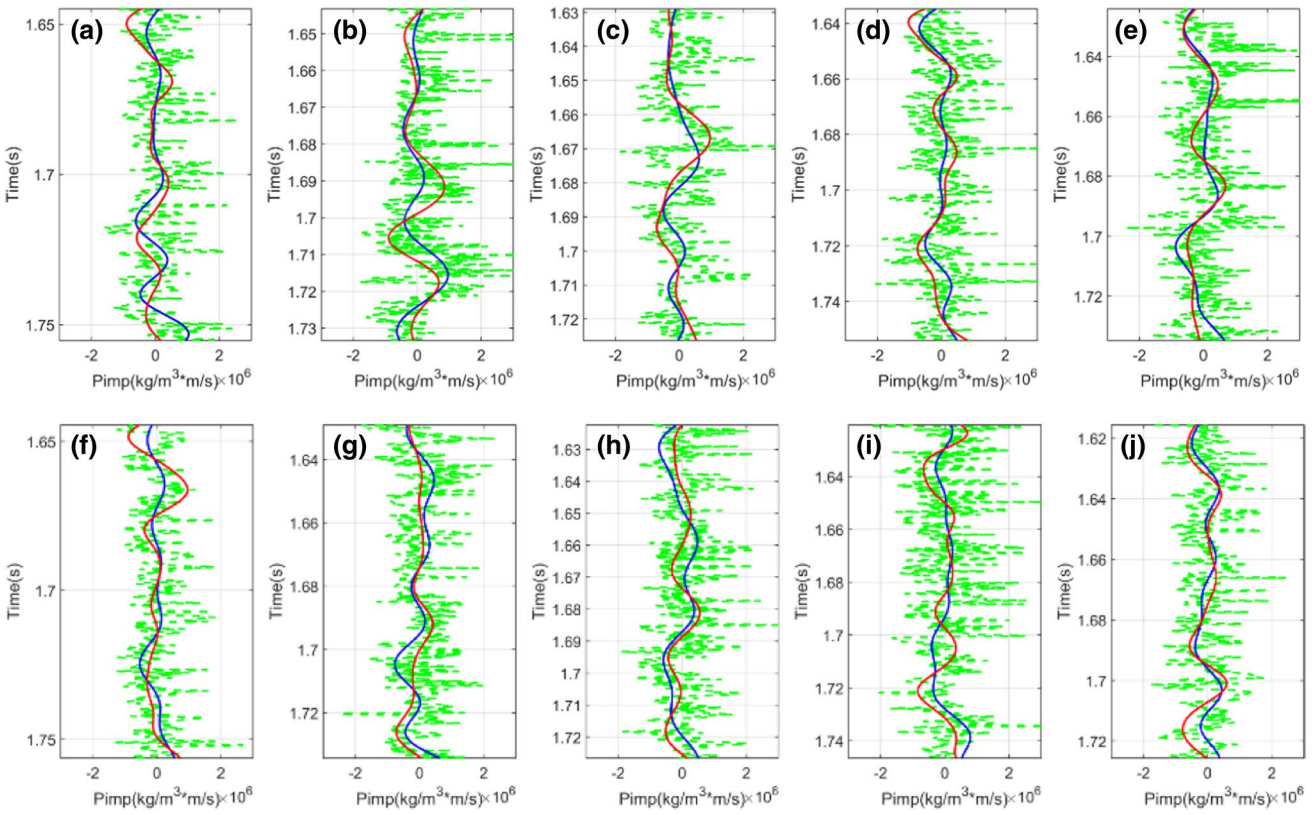

Fig. 11 Comparison between band-pass (12–45 Hz) I_p inverted from pre-stack seismic gather and band-pass (12–45 Hz) log curves. Note that the green dashed line denotes the original log curve with low-cut (12/2 Hz). The blue solid line indicates the original log curve with band-pass (12/2–45/5 Hz). The red solid line shows the inverted I_p from pre-stack band-pass seismic

in Table 2, which is comparable with that for the inverted band-pass I_p as shown in Fig. 11. It means that the prediction of low-frequency components from the band-pass dataset is reliable and trustable.

It is similar with I_p; here five wells A–E in Fig. 14a–e and five wells F–J in Fig. 14f–j are used to build a training model of V_p/V_s and to verify the model generalization capability. To obtain sufficient training samples, the following

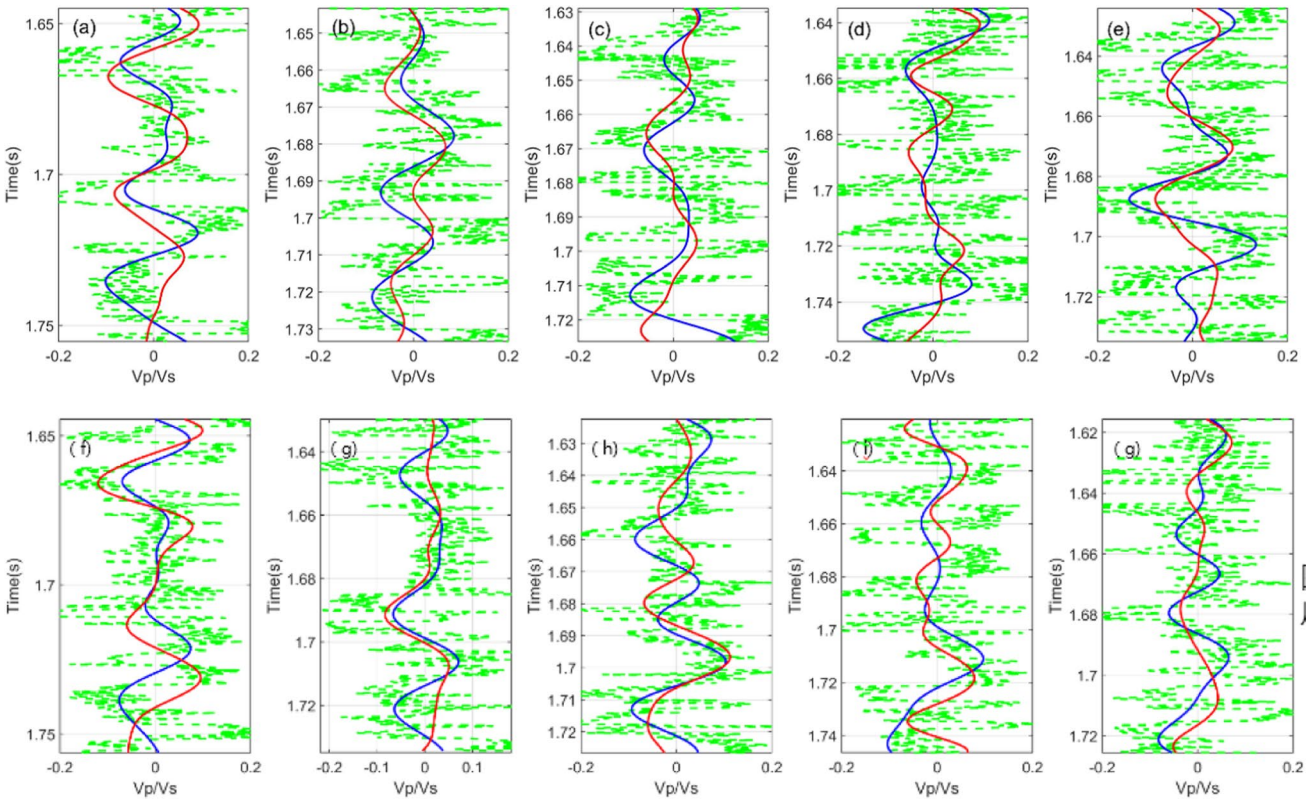

Fig. 12 Comparison between band-pass (12–45 Hz) V_p/V_s inverted from pre-stack seismic gather and band-pass (12–45 Hz) log curves. Note that the green dashed line denotes the original log curve with low-cut (12/2 Hz). The blue solid line indicates the original log curve with band-pass (12/2–45/5 Hz). The red solid line shows the inverted V_p/V_s from pre-stack band-pass seismic

six attributes translated from inverted band-pass V_p/V_s are selected. They are integrated (V_p/V_s_bp), quadrature trace (V_p/V_s_bp), amplitude weighted frequency (V_p/V_s_bp), filter 5/10–15/20 (V_p/V_s_bp) and $(V_p/V_s\_bp)^2$ because of high correlation comparing with those for low- and band-pass V_p/V_s_bp dataset. Table 3 shows the correlation between inverted low- and band-pass V_p/V_s_bp using DFNN (red) and low- and band-pass (45/5 Hz) V_p/V_s (blue). It suggests that the constructed model is reasonable and has strong generalization ability.

DFNN model application in field data

In this section, we use 3D band-pass elastic parameters from pre-stack constrained sparse spike inversion to predict low- and band-pass I_p and V_p/V_s profile using the proposed workflow. Figure 15a shows band-pass I_p results from a pre-stack constrained sparse spike inversion with crossing priori wells, while Fig. 15b shows low- and band-pass I_p results using the DFNN algorithm, which uses band-pass inversion results as an input. Well log curves in Fig. 15a, b are measured band-pass I_p and high-cut, respectively. The target zone is shaly sandstone formation, which is at deep depth and the late diagenetic stage. As a consequence, the I_p of sandstone is comparable with that of shale, causing weak comparability among wells. At the well site, pre-stack band-pass inverted I_p is similar to that from low- and band-pass I_p using the DFNN algorithm. However, differentiating from the "interbedded sand shale" feature in the vertical orientation observed from band-pass I_p (Fig. 15a), low- and band-pass I_p inverted from DFNN (Fig. 15b) exhibits strong structure characteristic, which is consistent with geological stratigraphy. The inverted I_p with blind wells in Fig. 16 shows a similar trend as Fig. 15 does.

Comparing to I_p, V_p/V_s is more sensitive to rock lithology. It is well known that sandstone exhibits low V_p/V_s, while shale rock has high V_p/V_s. Figure 17a, b shows band-pass V_p/V_s from pre-stack inversion and low- and band-pass V_p/V_s using DFNN with passing priori wells. Well log curves in Fig. 17a, b are measured band-pass V_p/V_s and high-cut V_p/V_s, respectively. It can observe that the low- and band-pass V_p/V_s seismic profile inverted from DFNN not only exhibits a strong formation structure but also appears lithology change and sand body pinching out laterally inside the rock formation, comparing with band-pass V_p/V_s profile from pre-stack constrained sparse spike inversion. Moreover, the stratigraphy feature of the sand body in the vertical

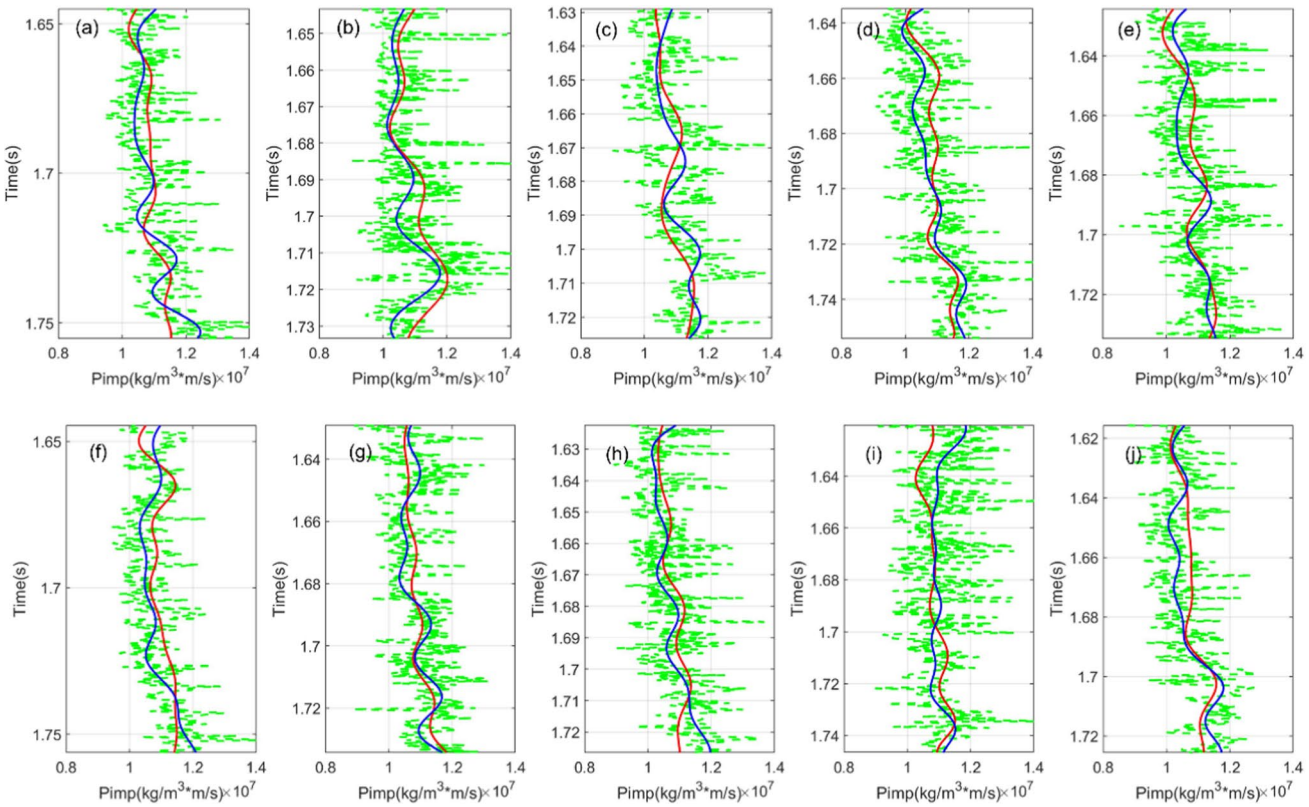

Fig. 13 Inverted I_p using DFNN algorithm with respect to band-pass I_p obtained by pre-stack inversion as input on (priori) training wells (**a**–**e**), and on (posterior) blinding wells (**f**–**j**). Note that green, blue, and red represents the original log curve, low- and band-pass (0–45 Hz) log curve, and low- and band-pass (0–45 Hz) I_p using DFNN prediction concerning band-pass I_p obtained by pre-stack inversion as input

orientation, lens shape of the sand body, and lateral stacking feature of the sand body are consistent with geological characteristics of braided channel sand body deposition. In addition, the inverted V_p/V_s with (posteriori) blind wells in Fig. 18 show a similar trend as Fig. 17 does.

More importantly, Fig. 19a, c shows that the "buphthalmos" artifact of I_p and V_p/V_s caused by well interpolation is strong. However, the DFNN algorithm dramatically decreases such artifacts. It is mainly because, for the conventional well interpolation method and DFNN-based inversion workflow, the input data of describing the lateral variation in low-frequency components of elastic parameters are different. Specifically, for the conventional well interpolation method, the lateral variation mainly depends on the number and distribution characteristics of well data points. When the distance among well points is larger than the lateral range, it will lead to the appearance of "buphthalmos" on the slice. It is well known that, compared with distance of hundreds or even thousands of meters between wells, the lateral sampling intervals of seismic data are only about 25 m. Therefore, using well interpolation method easily causes the "buphthalmos" phenomenon.

Different from the well interpolation method, transverse high-density seismic data are applied as an input in the DFNN-based inversion. Consequently, such high-density seismic data not only characterize transverse heterogeneity features but also maintain the continuity of elastic parameters. That is to say, DFNN-based inversion, to a certain degree, improves the resolution of inverted parameters slice. As a result, the V_p/V_s slice seems to look broken in Fig. 19d. Essentially, such "broken" V_p/V_s slice demonstrates the characteristics of multiple braided river systems in NW–SE

Table 2 Correlation coefficients between low- and band-pass I_p using DFNN prediction and high-cut logs

Log number	Correlation coefficient	Log number	Correlation coefficient
Well A	0.690	Well F	0.664
Well B	0.897	Well G	0.749
Well C	0.759	Well H	0.737
Well D	0.876	Well I	0.143
Well E	0.780	Well J	0.829

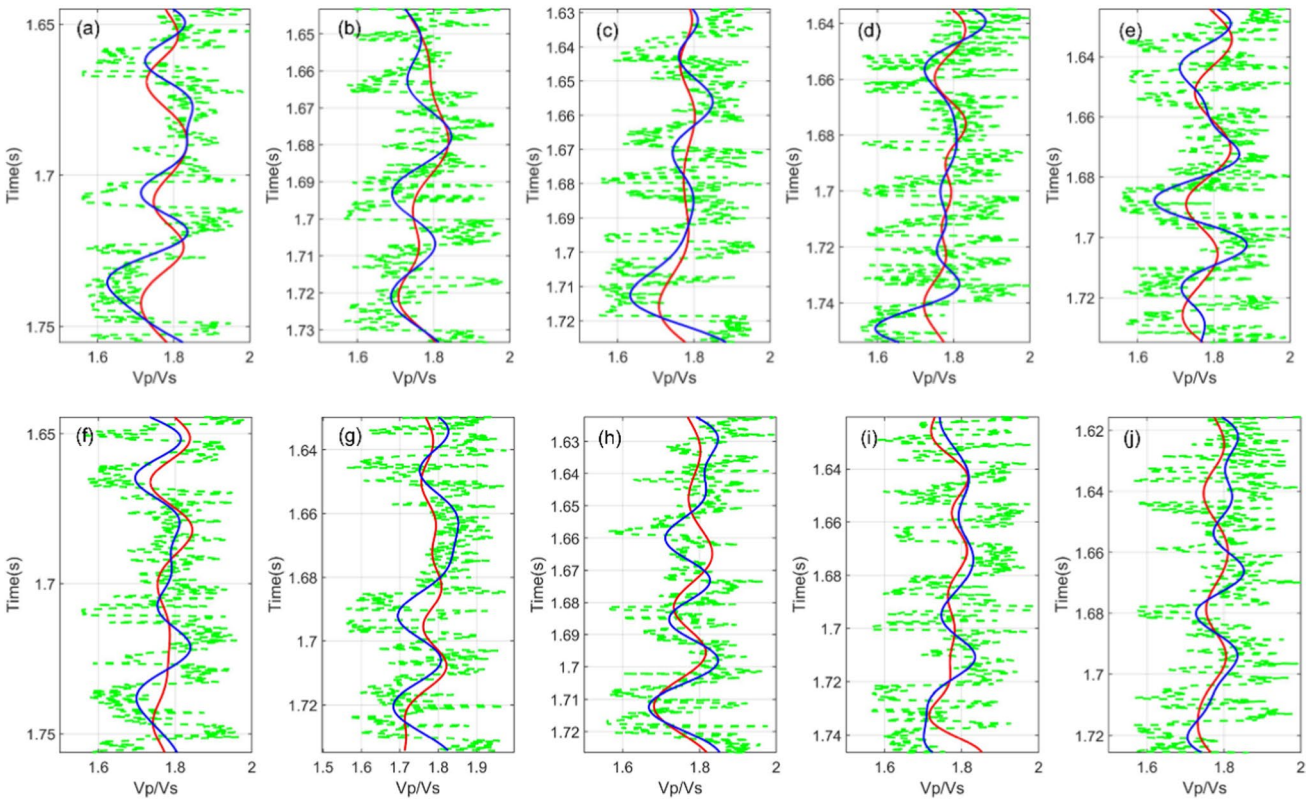

Fig. 14 Inverted V_p/V_s using DFNN algorithm with respect to band-pass V_p/V_s obtained by pre-stack inversion as input on (priori) training wells (**a**–**e**) and on (posterior) blinding wells (**f**–**j**). Note that green, blue, and red represent the original log curve, low- and band-pass (0–45 Hz) log curve, and low- and band-pass (0–45 Hz) V_p/V_s using DFNN prediction concerning band-pass V_p/V_s obtained by pre-stack inversion as input

strike, which is consistent with the geological understanding of the sedimentary environment.

Conclusions

In this paper, we aim to reconstruct the missing low frequencies, using an artificial neural network, which is a promising data-driven approach within the machine learning framework.

Table 3 Correlation coefficients between low- and band-pass V_p/V_s using DFNN prediction and high-cut logs

Log number	Correlation coefficient	Log number	Correlation coefficient
Well A	0.574	Well F	0.624
Well B	0.725	Well G	0.513
Well C	0.763	Well H	0.573
Well D	0.630	Wel lI	0.500
Well E	0.657	Well J	0.707

Taking into account the spatial complexity of elastic characteristics of the low frequency of the dataset, the abundance of model training samples, and the noise level of training data, the DFNN algorithm is applied to estimate low- and band-pass elastic attributes from band-pass elastic attributes.

For the 1D blind well test, the low-frequency content predicted by DFNN is consistent with practical one in 5 (posteriori) blind wells, suggesting the feasibility and generality of the proposed AVO inversion-DFNN hybrid algorithm. Moreover, for the 2D seismic profile application, the low-frequency component of elastic attributes using DFNN prediction clearly reflects the horizontal deposition trend and the diagenesis trend in the vertical orientation. Overall, this smooth variation feature captured by DFNN in the space domain, instead of space distortion, is more reasonable according to geological diagenesis.

Appendix A

This appendix differentiates the regularization term $R(m)$ in Eq. 6. $R(m)$ can be written as:

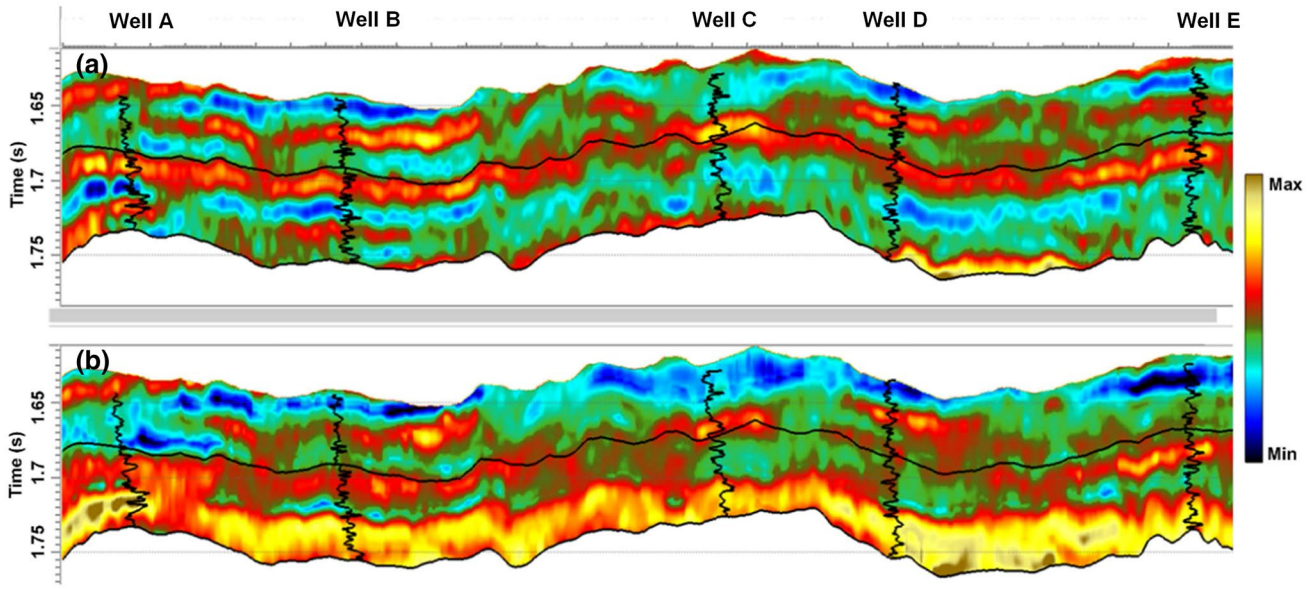

Fig. 15 I_p Profile with (priori) training wells. **a** Band-pass I_p profile from pre-stack constrained sparse spike inversion. The black curve is the original band-pass (12–45 Hz) I_p log curve; **b** low- and band-pass (0–45 Hz) I_p profile from DFNN prediction using inverted band-pass I_p (Fig. 13a) as input. The black curve is a high cut (45/5 Hz) I_p log curve

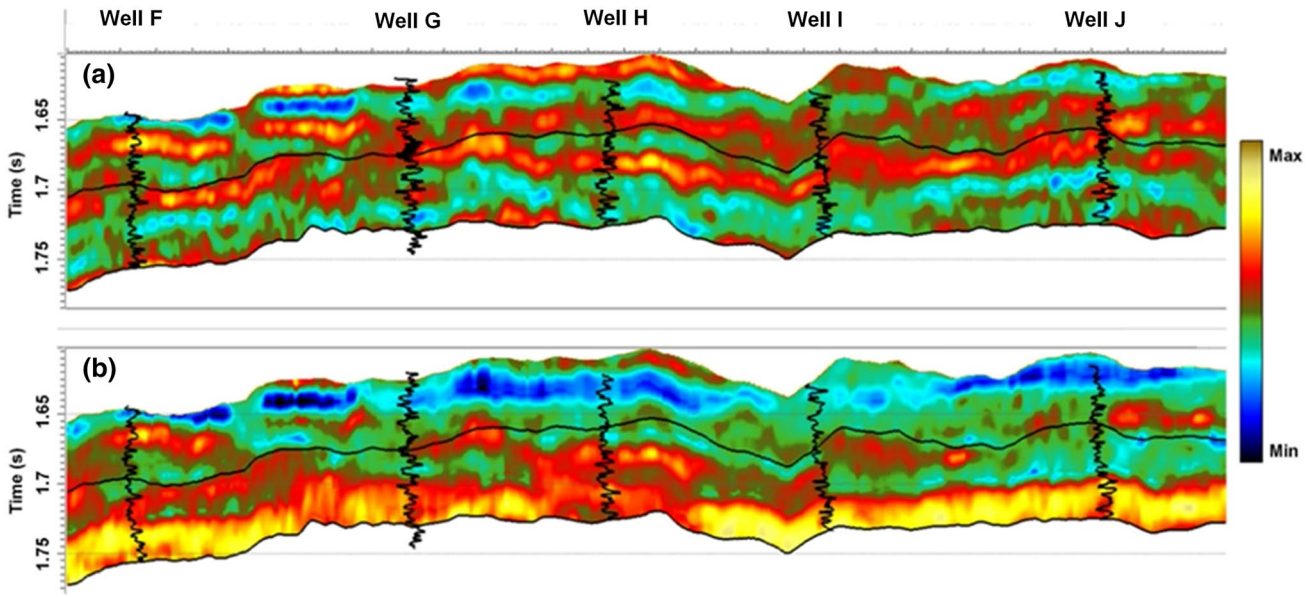

Fig. 16 I_p Profile with (posterior) blind wells. **a** Band-pass I_p profile from pre-stack constrained sparse spike inversion. The black curve is the original band-pass (12–45 Hz) I_p log curve; **b** low- and band-pass (0- 45 Hz) I_p profile from DFNN prediction using inverted band-pass I_p (Fig. 14a) as input. The black curve is a high cut (45/5 Hz) I_p log curve

$$\frac{\partial R(\mathbf{m})}{\partial \mathbf{m}} = \left[\frac{\partial R(\mathbf{m})}{\partial m_1} \cdots \frac{\partial R(\mathbf{m})}{\partial m_k} \cdots \frac{\partial R(\mathbf{m})}{\partial m_{3N}}\right]^T. \tag{17}$$

Taking the derivative of $R(m)$ with respect to m_k, then we can get:

$$\frac{\partial R(\mathbf{m})}{\partial m_k} = 2\sum_{i=1}^{N}\left(\frac{1}{1+\mathbf{m}^T\boldsymbol{\Phi}^i\mathbf{m}}\right)\frac{\partial}{\partial m_k}\mathbf{m}^T\boldsymbol{\Phi}^i\mathbf{m}. \tag{18}$$

If expanding the second term of Eq. (18), then we have:

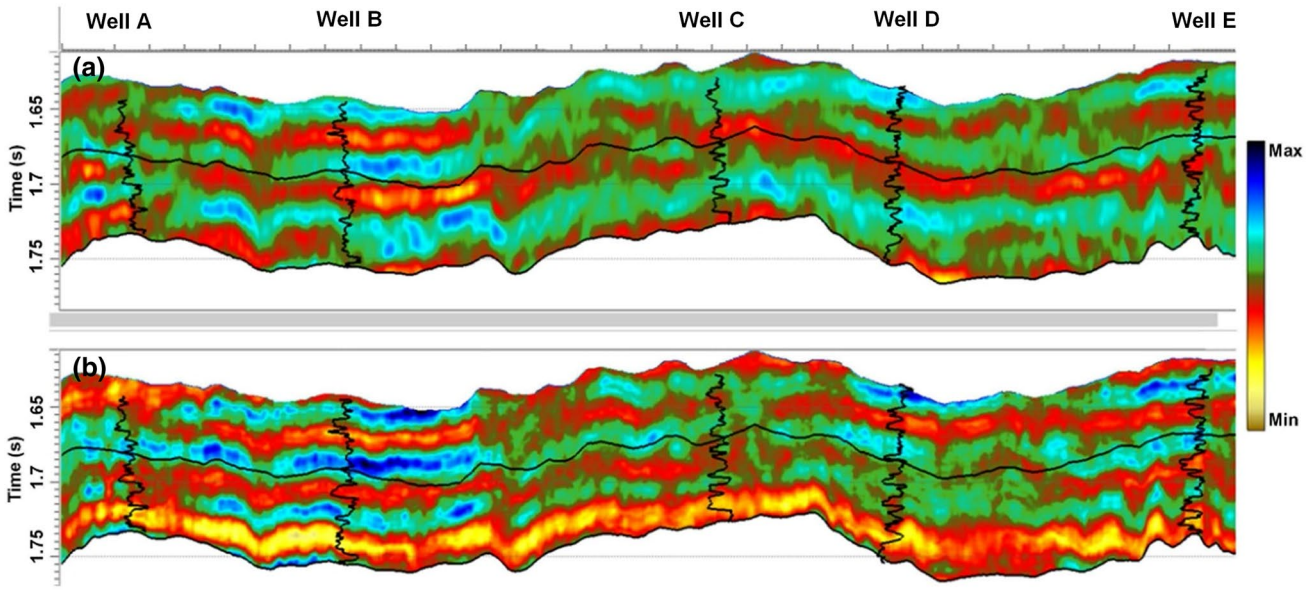

Fig. 17 V_p/V_s Profile with (priori) training wells. **a** Band-pass V_p/V_s profile from pre-stack constrained sparse spike inversion. The black curve is the original band-pass (12–45 Hz) V_p/V_s log curve; **b** low- and band-pass (0–45 Hz) V_p/V_s profile from DFNN prediction using inverted band-pass V_p/V_s (Fig. 13a) as input. The black curve is a high cut (45/5 Hz) V_p/V_s log curve

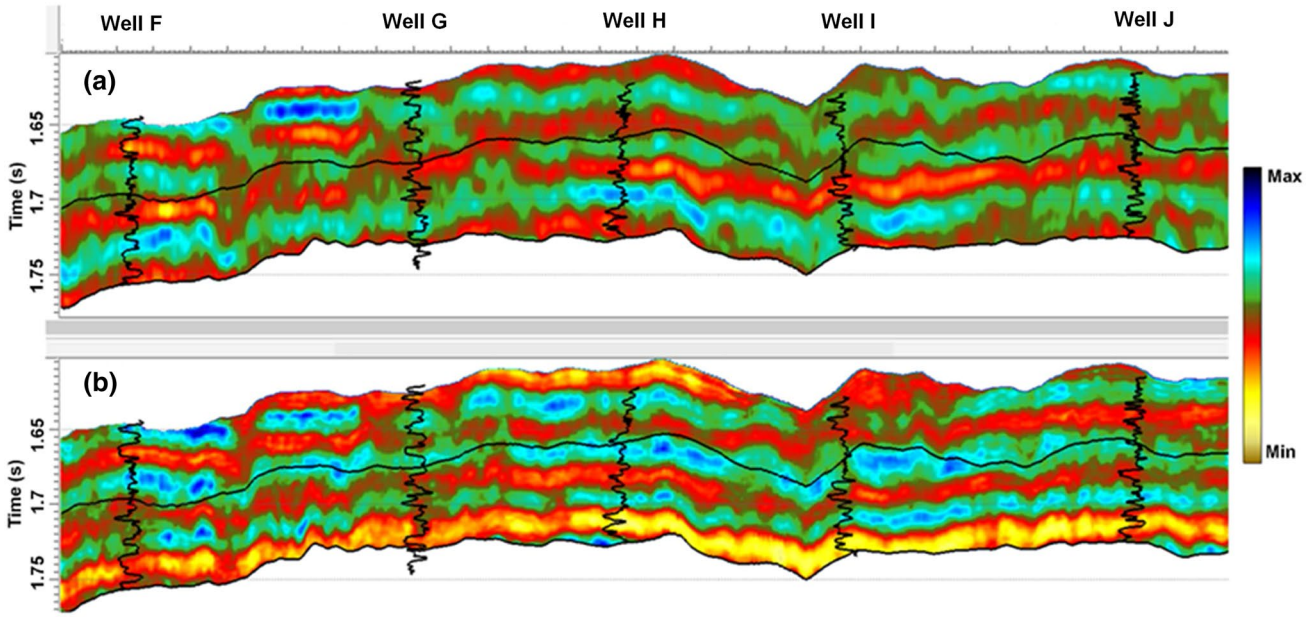

Fig. 18 V_p/V_s Profile with (posterior) blind wells. **a** Band-pass V_p/V_s profile from pre-stack constrained sparse spike inversion. The black curve is the original band-pass (12–45 Hz) V_p/V_s log curve; **b** low- and band-pass (0–45 Hz) V_p/V_s profile from DFNN prediction using inverted band-pass V_p/V_s (Fig. 16a) as input. The black curve is a high cut (45\5 Hz) V_p/V_s log curve

$$\frac{\partial R(\mathbf{m})}{\partial m_k} = 2\sum_{i=1}^{N}\left(\frac{1}{1+\mathbf{m}^T\boldsymbol{\Phi}^i\mathbf{m}}\right)\frac{\partial}{\partial m_k}\left(\sum_{l=1}^{3N}\sum_{N=1}^{3N} m_l m_n \boldsymbol{\Phi}^i_{\ln}\right). \tag{19}$$

By using the fact $\frac{\partial m_p}{\partial m_q} = \delta_{pq}\begin{cases} = 1, \text{ if } p = q \\ = 0, \text{ if } p \neq q \end{cases}$, Eq. (19) can be written as:

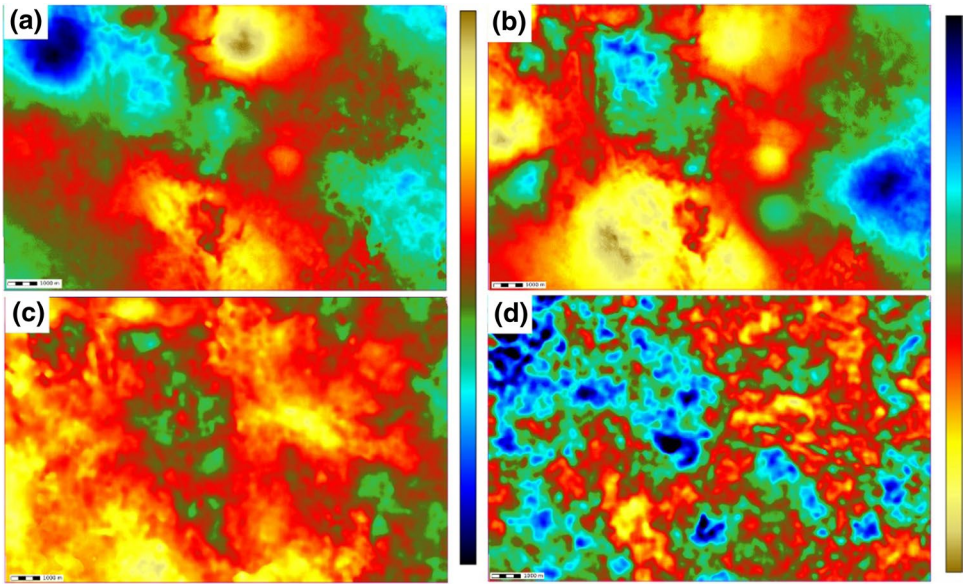

Fig. 19 **a** Low-frequency I_p, and **b** V_p/V_s estimated from well interpolation, **c** low I_p, and **d** V_p/V_s predicted from the DFNN-based method

$$\frac{\partial R(\mathbf{m})}{\partial m_k} = 2\sum_{i=1}^{N}\left(\frac{2\sum_{l=1}^{3N} m_n \mathbf{\Phi}_{kn}^{i}}{1+\mathbf{m}^T\mathbf{\Phi}^i\mathbf{m}}\right). \tag{20}$$

After changing the order of summation of Eq. (20), then:

$$\frac{\partial R(\mathbf{m})}{\partial m_k} = 2\sum_{i=1}^{3N}\left(\sum_{l=1}^{N}\frac{2\mathbf{\Phi}_{kn}^{i}}{1+\mathbf{m}^T\mathbf{\Phi}^i\mathbf{m}}\right)m_n = 2\sum_{i=1}^{3N}\Phi_{kn}m_n, \tag{21}$$

where $Q_{kn} = \sum_{i=1}^{N}\frac{2\mathbf{\Phi}_{kn}^{i}}{1+\mathbf{m}^T\mathbf{\Phi}^i\mathbf{m}}$, $k, n = 1, 2, 3, \ldots, 3N$.

Author contributions XM contributed to the conception of the study; XH and BW performed the experiment; ZW contributed significantly to analysis and manuscript preparation; HZ performed the data analyses and wrote the manuscript; HW and XM helped perform the analysis with constructive discussions.

Funding None.

Declarations

Conflict of interest All authors declares that they have no conflict of interest.

Ethics approval All authors approve that this paper has not been submitted or published anywhere.

Consent to participation All authors consent to participate in this work.

Consent for publication All authors consent to publish this work.

References

Alfarraj M, AlRegib G (2019) Petrophysical property estimation from seismic data using recurrent neural networks. Available online at: arxiv:1901.08623

Araya-Polo M, Jennings J, Adle A, Dahlke T (2018) Deep-learning tomography. Lead Edge 37(1):58–66

Ball V, Blangy JP, Schiott C, Chaveste A (2014) Relative rock physics. Lead Edge 33(3):276–286

Biswas R, Sen MK, Das V, Mukerji T (2019) Prestack and post stack inversion using a physics-guided convolutional neural network. Interpretation 7(3):SE161–SE174

Buland A, Omre H (2003) Bayesian linearized AVO inversion. Geophysics 68:185–198

Caers J (2011) Modeling uncertainty in the earth sciences. Wiley, Chichester

Connolly P (1999) Elastic impedance. Lead Edge 18(4):438–438

Das V, Mukerji T (2020) Petrophysical properties prediction from prestack seismic data using convolutional neural networks. Geophysics 85(5):N41–N55

Das V, Pollack A, Wollner U, Mukerji T (2019) Convolutional neural network for seismic impedance inversion. Geophysics 84(6):R869–R880

Debeye HWJ, Vanriel P (1990) Lp-Norm deconvolution. Geophys Prosp 38(4):381–403

Deutsch CV (2002) Geostatistical reservoir modeling. Oxford University Press, New York

Di H, Chen X, Maniar H, Abubakar A (2020) Semi-supervised seismic and well log integration for reservoir property estimation. In: SEG program expanded abstracts, 2166–2170

Doyen PM, Guidish TM (1992) Seismic discrimination of lithology: a Monte Carlo approach. In R. E. Sheriff, (ed.), Reservoir geophysics: SEG, 243–250

Eidsvik J, Avseth P, Omre H, Mukerji T, Mavko G (2004) Stochastic reservoir characterization using prestack seismic data. Geophysics 69:978–993

Eidsvik J, Mukerji T, Bhattacharjya D (2015) Value of information in the earth sciences, (integrating spatial modeling and decision analysis). Cambridge University Press, London

Goodfellow I, Bengio Y, Courville A (2016) Deep learning. MIT Press, Boston

Grana D, Verma S, Pafeng J, Lang X, Sharma H, Wu W, Campbell-Stone E, Ng K, Alvarado V, Mallick S, Kaszuba J (2017) A rock physics and seismic reservoir characterization study of the rock springs uplift, a carbon dioxide sequestration site in Southwestern Wyoming. Int J Greenhouse Gas Control 63:296–309. https://doi.org/10.1016/j.ijggc.2017.06.004

Hampson DP, Russel BH (2005) Simultaneous inversion of prestack seismic data. In: 75th Annual international meeting, SEG, expanded abstracts 1633–1637

Kelly M (2001) AVO inversion, part 1: isolating rock property contrasts. Geophysics 20(3):320

Krizhevsky A, Sutskever I, Hinton G (2012) ImageNet classification with deep convolutional neural networks. Adv Neural Inf Process Syst 25:1097–1105

LeCun Y, Bengio Y, Hinton G (2015) Deep learning. Nature 521:436–444. https://doi.org/10.1038/nature14539

Li H, Lin J, Wu BH, Gao JH, Liu NH (2021) Elastic properties estimation from prestack seismic data using GGCNNs and application on tight sandstone reservoir characterization. IEEE Trans Geosci Remote Sens 60:1–21

Lopez-Moreno I, Gonzalez-Dominguez J, Martinez D (2016) On the use of deep feedforward neural networks for automatic language identification. Comput Speech Lang 40:46

Mesdag PR, Marquez D, de Groot L, Aubin V (2010) Updating low frequency model. In: 72nd EAGE conference and exhibition incorporating SPE EUROPEC, Barcelona

Monajemi H, Donoho DL, Stodden V (2016) Making massive computational experiments painless: big data, 2368–2373

Mukerji T, Jørstad A, Avseth P, Mavko G, Granli JR (2001) Mapping lithofacies and pore-fluid probabilities in a North Sea reservoir: seismic inversions and statistical rock physics. Geophysics 66:988–1001

Peters B, Granek J, Haber E (2019) Multi-resolution neural networks for tracking seismic horizons from few training images. Interpretation 7(3):1–54. https://doi.org/10.1190/int-2018-0225.1

Richardson A (2018) Seismic full-waveform inversion using deep learning tools and techniques. http://arxiv.org/abs/1801.07232

Russell BH, Gray D, Hampson DP (2011) Linearized AVO and poroelasticity. Geophysics 76(3):C19–C29

Yuan SY, Wang SX, Luo YE, Wei WW, Wang GC (2019) Impedance inversion by using the low-frequency full-waveform inversion result as an a priori model. Geophysics 84:R149–R164

Yuan SY, Jiao XQ, Luo YE, Sang WJ, Wang XS (2021) Double-scale supervised inversion with a data-driven forward model for low-frequency impedance recovery. Geophysics 0:1–102

Zheng Y, Zhang Q (2018) Pre-stack seismic inversion using deep learning. In: Presented at 1st EAGE/PESGB workshop on machine learning. Downloaded 07/30/19 to 180.101.128.24